Detection limits of volcanic SO_2 in Earth's atmosphere obscured by scattering

Author: Daniel Hague
Project Number: AO13
Supervisors: Dr A. Knizek, Prof R. G. Grainger

Abstract

Volcanic SO_2 monitoring is complicated by the presence of scattering aerosols co-injected during the eruption, which attenuate the observed infrared signal and raise the effective detection threshold. This project uses the Scattering Reference Forward Model (SRFM) to simulate IASI brightness temperature spectra across a range of SO_2 column amounts and volcanic aerosol loadings, quantifying the impact of scattering on SO_2 in the ν_1 window (1000–1200 cm^{-1}). Simulations are motivated by the January 2022 Hunga Tonga–Hunga Ha'apai eruption, incorporating H_2SO_4 aerosol, volcanic ash and stratospheric water ice as scatterer species. Simulations across a systematic range of SO_2 column amounts in a clean background atmosphere establish a 3σ detection limit of 11.7 Dobson units (DU), which increases to 14.6 DU under a realistic volcanic scattering scenario. Of the three scatterer species, H_2SO_4 aerosol produces the dominant signal suppression, with volcanic ash having a moderate effect and stratospheric water ice having a negligible impact. Applied to four Hunga Tonga plume scenarios, IASI is found to reliably detect 30 DU SO_2 columns under complex scattering, while a 10 DU plume-edge scenario falls below the detection threshold. These results highlight the importance of scattering corrections for marginal plumes and identify sulphuric acid aerosol characterisation as the key priority for accurate infrared SO_2 retrievals.

1 Introduction

Volcanic eruptions inject large quantities of material into the atmosphere, with impacts that extend far beyond the immediate eruption site. Volcanic plumes consist of particulates such as volcanic ash, alongside gases including CO_2, SO_2, and water vapour. These emissions can have widespread effects: particulates disrupt aviation operations, while SO_2 undergoes oxidation to form sulphuric acid aerosol, leading to short-term global radiative cooling on the scale of one to three years [1].

Satellite instruments can monitor volcanic SO_2 by detecting its spectral absorption signature within Earth's emitted radiation. However, these measurements are complicated by atmospheric scattering. Rayleigh scattering by air molecules dominates in the ultraviolet (UV), while Mie scattering by volcanic aerosols and particulates dominates at visible and infrared wavelengths. Accounting for scattering is therefore essential for accurate SO_2 retrievals, and by extension for constraining the sulphuric acid aerosol burden that drives volcanic radiative forcing.

This report focuses on the January 2022 Hunga Tonga–Hunga Ha'apai eruption, one of the most explosive volcanic events ever observed [2]. The eruption injected exceptional quantities of SO_2, volcanic ash, and water vapour into the stratosphere, with the SO_2 rapidly oxidising to form sulphuric acid aerosol, producing an extreme scattering environment in which initial satellite retrievals underestimated the SO_2 column amount. This eruption therefore provides a physically motivated test case for quantifying the impact of scattering on SO_2 detection limits. Using the Scattering Reference Forward Model (SRFM) [3] to simulate brightness temperature spectra observable by the Infrared Atmospheric Sounding Interferometer (IASI) [4], this report quantifies detection limits across a range of SO_2 column amounts and volcanic aerosol configurations, aiming to isolate the role of atmospheric scattering in determining the effective detection limit of SO_2 in the infrared.

2 Method

2.1 The Scattering Reference Forward Model

The Scattering Reference Forward Model is a package that provides a reference forward model for the calculation of spectra including both absorption and scattering [3]. It consists of three external codes, the Reference Forward Model (RFM), Discrete Ordinate Radiative Transfer (DISORT), and mie_ewp. The RFM is a radiative transfer code which calculates gas absorption within the atmosphere from an inputted atmospheric profile, viewing geometry and spectral resolution [5]. DISORT is a code that calculates radiative transfer with scattering [6], and mie_ewp is a code that calculates Mie scattering on particles. The SRFM runs the RFM code first, then the Mie code, with the outputs from both of these being used in DISORT to produce the final spectrum of brightness temperature or spectral radiance against wavenumber.

The SRFM is run using a driver table that has inputs for each code package. The RFM reads the atmospheric profile, as well as other flags which will be unchanged throughout. It also reads key spectroscopic data for each atmospheric gas included with the calculation from the 2020 HITRAN

database [7]. The only RFM input modified between simulations was whether to include SO_2 within the atmospheric profile or not. The DISORT configuration is also part of the driver table, but these inputs were unchanged as well. The final part of the driver table is the scattering configuration, which contains the inputs for the Mie code. It contains a list of the scatterers, their individual properties, as well as the height of each layer. The scatterers used were sulphuric acid aerosol, volcanic ash and water ice. In order to model the scattering conditions, the following scatterer inputs were varied between simulations: height, mean radius, and mass loading. Refractive indices of each aerosol are also required inputs for this part of the driver table and are taken from the ARIA database [8], which provides refractive index data at each wavenumber for each aerosol being modelled. The resolution of the SRFM is also set in the driver table, as well as the wavenumber range to be modelled over, allowing the user to increase the resolution of the spectrum and also change what regime is being modelled. The SRFM was therefore run across the wavenumber range observed by IASI in which there is significant SO_2 absorption, 645–1500 cm^{-1}.

2.2 Volcanic Scenario

The aim of this report is to model atmospheric conditions representative of the 15th January 2022 eruption of Hunga Tonga–Hunga Ha'apai, which injected large amounts of SO_2 and aerosols into the upper troposphere and lower stratosphere [9].

A single daytime tropical atmospheric profile was used, taken from the MIPAS model atmospheres for January 2001 [10], consistent with the location of the eruption (20.5° S, 175.4° W). All non-SO_2 trace gas profiles were held constant across simulations. While the eruption also injected an exceptional quantity of water vapour directly into the stratosphere [11], this report focused specifically on the role of volcanic aerosol scattering on SO_2 detection. As the background profile was initially for 2001, CO_2 concentrations were scaled uniformly by the percentage increase in mean atmospheric CO_2 concentrations between 2001 and 2022 levels [12], to better represent conditions at the time of the eruption.

Satellite observations indicate that the eruption primarily injected SO_2 into the stratosphere, with the bulk of the column observed around 25 km [13]. SO_2 concentrations were therefore incorporated into the atmospheric profile consistent with height, between 23 and 25 km. To characterise the effects of stratospheric aerosol scattering, the June 2019 eruption of Raikoke volcano was used as a reference case, with aerosol mass loadings taken from [14]. Six simulation sets were run, summarised in Table 1.

Table 1: Summary of simulation sets. All sets use the four-run A/B/C/D structure described in Table 2. "Fixed" scattering refers to the Raikoke-based configuration described in Section 2.3.

Set	SO_2 column (DU)	Scattering	Purpose
1	10, 20, 25, 30, 50	None	Clean atmosphere detection-limit baseline
2	30 (fixed)	H_2SO_4 sweep (0.01–1.0 $\mathrm{g\,m^{-2}}$)	Sulphuric acid loading sensitivity
3	30 (fixed)	Ash sweep (0.01–1.0 $\mathrm{g\,m^{-2}}$)	Volcanic ash loading sensitivity
4	30 (fixed)	Strat. water ice sweep (0.01–1.0 $\mathrm{g\,m^{-2}}$)	Stratospheric water ice sensitivity
5	10, 20, 25, 30, 50	Fixed (Raikoke-based)	Scattered atmosphere detection-limit
6	10 or 30	Fixed (HT scenario configs)	Hunga Tonga plume scenarios

For each model configuration, four simulations were run in which SO_2 presence and scattering conditions were varied independently, as summarised in Table 2. All other variables were held constant across these four simulations, ensuring that only SO_2 absorption and scattering affected the resulting spectra.

Table 2: Four-run structure used for each model configuration. The paired differences isolate the SO_2 signal in the scattered and clean atmospheres respectively, as described in Section 2.5.

Run	SO_2 present	Scattering present	Role
A	Yes	Yes	Signal + scattering
B	Yes	No	Signal, clean atmosphere
C	No	Yes	Scattering reference
D	No	No	Clean atmosphere reference
Paired differences: $\Delta BT_{\text{scattered}} = A - C$; $\Delta BT_{\text{clean}} = B - D$			

2.3 Aerosol and Cloud Scattering Representations

Following the eruption of Hunga Tonga, vast quantities of ash, water and SO_2 were injected into the atmosphere. Typically, conversion of SO_2 to H_2SO_4 has an e-folding time of 1 month [15], however for this eruption significant quantities of H_2SO_4 were observed within a few days [2], owing to the anomalous stratospheric water injection. Three scatterer species were therefore included: sulphuric acid (H_2SO_4), volcanic ash, and water ice. H_2SO_4 was placed between 23 and 24 km, ash between 22 and 23 km, and stratospheric water ice between 26 and 27 km. A tropospheric water layer was also included at 2–3 km, with a fixed mass loading of 100 g m^{-2} across all simulations, representing a background cloud layer. As the SRFM does not allow scatterer layers to overlap with one another, the ash and sulphuric acid aerosol layers—which satellite observations indicate to be co-located—were simulated as adjacent layers, just below the injected SO_2. A second set of simulations was run with these two layers swapped in order to test sensitivity to layer ordering, with results not significantly affected.

For scatterer loading sweeps (Sets 2, 3 and 4), the mass loading of each species was independently varied across 0.01, 0.1, 0.2, 0.5 and 1.0 g m^{-2}, while all other scatterer loadings were held constant, allowing the sensitivity of the SO_2 signal to each individual species to be isolated.

2.4 IASI and SO_2 Detection

SO_2 has two main vibrational bands in the infrared that are relevant to satellite remote sensing: the ν_1 symmetric stretching band centred near 1150 cm^{-1} (1000–1200 cm^{-1}), and the stronger ν_3 asymmetric stretching band centred near 1360 cm^{-1}. This study uses the ν_1 window as the primary analysis region, consistent with the standard operational window used in IASI SO_2 retrievals [16].

SRFM simulations were run over the infrared spectral range, at a high spectral resolution of 0.01 cm^{-1}. The resulting spectra were then convolved with the IASI instrument line shape, which has a resolution of 0.25 cm^{-1}. Channel-dependent IASI noise equivalent differential temperature (NEDT) data, which represents the smallest temperature change within the atmosphere that the IASI satellite can detect above its background noise, was then interpolated onto the SRFM wavenumber grid. This represents the error of the IASI instrument on each wavenumber channel, and was used as the 1σ noise for all downstream calculations.

2.5 SO_2 signal

The spectral signature of SO_2 was isolated using paired brightness temperature differences between simulations run under identical atmospheric and scattering conditions, differing only in the presence or absence of SO_2. For simulations with scattering enabled, the SO_2 signal was defined as:

$$\Delta \mathrm{BT}_{scattered}(\nu_i) = \mathrm{BT_A}(\nu_i) - \mathrm{BT_C}(\nu_i) \tag{1}$$

where A denotes the simulation with SO_2 and scattering present, and C denotes the simulation with scattering present but no SO_2. For simulations with scattering disabled, the equivalent clean atmosphere signal was defined as:

$$\Delta \mathrm{BT}_{\mathrm{clean}}(\nu_i) = \mathrm{BT_B}(\nu_i) - \mathrm{BT_D}(\nu_i) \tag{2}$$

where B denotes the simulation with SO_2 but no scattering, and D denotes the simulation with neither SO_2 nor scattering.

In both cases, subtracting the run without SO_2 from the run with SO_2 isolates the SO_2 absorption feature. Comparison of $\Delta \mathrm{BT}_{scattered}$ and $\Delta \mathrm{BT}_{clean}$ for the same SO_2 column then directly quantifies the effect of scattering on the detectability of SO_2.

2.6 Detection Criteria

Detection of SO_2 was evaluated using a 3σ signal-to-noise criterion, consistent with detection criteria for satellite-based remote sensing. Under the assumption of Gaussian noise, this ensures that the

signal is statistically distinguishable from random measurement fluctuations and is unlikely to arise from noise alone.

For each instrument channel ν_i, the signal-to-noise ratio (SNR) was defined as

$$\mathrm{SNR}(\nu_i) = \frac{\Delta BT(\nu_i)}{\sigma(\nu_i)}, \tag{3}$$

where $\Delta BT(\nu_i)$ is the differential brightness temperature defined in Section 2.5 and $\sigma(\nu_i)$ represents the one-standard-deviation measurement uncertainty for that channel. For IASI, $\sigma(\nu_i)$ corresponds to the channel-dependent NEDT.

A detection was considered to occur when

$$\mathrm{SNR}(\nu_i) \geq 3. \tag{4}$$

2.7 Simulation sets

Six sets of simulations were run in total, each isolating a specific aspect of the scattering detection problem, summarised in Table 1. All sets used the four-run A/B/C/D structure described in Section 2.2 (Table 2), with the SO_2 signal extracted as described in Section 2.5. Sets 1 and 5 establish the clean and scattered detection limit baselines respectively, by sweeping SO_2 column amount across 10, 20, 25, 30 and 50 DU. Sets 2, 3 and 4 each fixed the SO_2 column at 30 DU, and independently varied the mass loading of a single scatterer species across 0.01, 0.1, 0.2, 0.5 and 1.0 $\mathrm{g\,m^{-2}}$, while holding all other scatterer loadings constant, isolating the sensitivity of the SO_2 signal to each species in turn.

Set 6 comprised four simulations using fixed scatterer configurations representative of distinct plume conditions during the January 2022 Hunga Tonga eruption, detailed in Table 3.

Table 3: Set 6 Hunga Tonga scenario configurations. All scenarios include a fixed tropospheric water layer at 2–3 km (100 $\mathrm{g\,m^{-2}}$). H_2SO_4 is placed at 23–24 km, ash at 22–23 km, and stratospheric water ice at 26–27 km.

Scenario	SO_2 (DU)	H_2SO_4 ($\mathrm{g\,m^{-2}}$)	Ash ($\mathrm{g\,m^{-2}}$)	Strat. H_2O ($\mathrm{g\,m^{-2}}$)	Description
6.1	30	0.10	0.01	0.10	Plume centre; reference case
6.2	30	0.20	0.21	0.50	Dense plume; peak aerosol and water loading
6.3	10	0.05	0.01	0.10	Plume edge; reduced SO_2
6.4	30	0.10	0.01	0.50	As 6.1; elevated stratospheric water only

3 Results

3.1 Spectral signature of SO_2

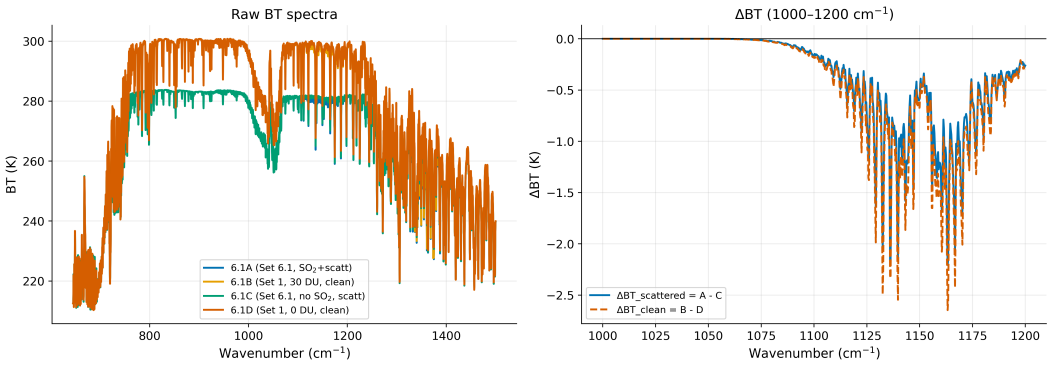

Figure 1: (*a*) Raw brightness temperature spectrum for the Hunga Tonga Set 6.1 scenario across the full SRFM wavenumber range (645–1500 $\mathrm{cm^{-1}}$). Runs A and C include scattering, runs B and D are scattering free. A and C contain SO_2 and no SO_2 respectively; B and D are the corresponding clean atmosphere equivalents taken from Set 1 at 30 DU and 0 DU.
(*b*) Differential brightness temperature (ΔBT) in the SO_2 ν_1 window (1000–1200 $\mathrm{cm^{-1}}$) for the Set 6 scenario.

Figure 1 shows the raw brightness temperature spectra for the central Hunga Tonga eruption scenario, illustrating the impact of SO_2 absorption and scattering on the observed signal. Four simulation runs are presented in plot (a): SO_2 with scattering (A), SO_2 without scattering (B), background atmosphere

with scattering (C), and the background atmosphere without scattering (D). A clear absorption feature is present in the 1000–1200 cm^{-1} region, consistent with SO_2 absorption.
Plot (b) isolates the SO_2 contribution by differencing the paired simulations, zoomed into the key absorption region. The signal in the scattering case is reduced in magnitude compared with the non-scattering case. This indicates that scattering suppresses the observable SO_2 brightness temperature contrast and spectrum. Overall, Figure 1 shows that scattering noticeably weakens the SO_2 signal. This is important because it reduces the margin between the signal and the instrument noise, directly affecting the detection limit.

3.2 Hunga Tonga scenario spectra relative to instrument noise

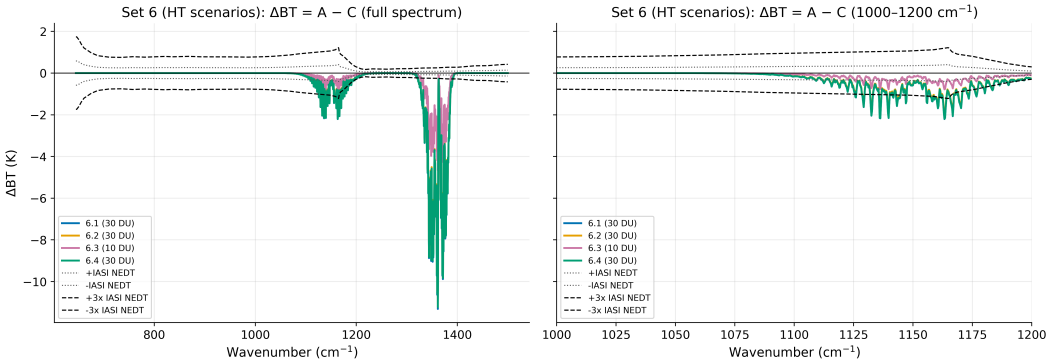

Figure 2: ΔBT for all Set 6 (Hunga Tonga) scenarios, shown across the full spectrum (left) and zoomed into the SO_2 ν_1 window (right). Dashed black lines indicate the $\pm 3\sigma$ ($3 \times$ NEDT) detection threshold. Dotted grey lines indicate $\pm 1\sigma$ (NEDT).

To assess detectability under Hunga Tonga-like atmospheric conditions, scenario runs were analysed using the scattering-sensitive signal definition (1) where A and C are paired runs under identical atmospheric and plume conditions. Figure 2 presents these ΔBT spectra across the full simulated infrared range, and separately as a zoom on the principal SO_2 absorption region. The channel-dependent IASI NEDT, interpolated onto the SRFM grid, is overlaid as both $\pm$NEDT and $\pm 3 \times$ NEDT reference envelopes.
Across the spectrum, the scenario curves are structured and distinct, but the most diagnostically relevant behaviour is concentrated within the SO_2 window, where the 3σ detection threshold is exceeded. In the 1000–1200 cm^{-1} plot, the differences between the scenarios are clearer: the 30 DU cases (6.1, 6.2 and 6.4) are of similar magnitude, generally larger than the 10 DU case, consistent with the lower SO_2 burden at the edge of the plume. Comparison against the $3 \times$ NEDT envelopes provides a direct 3σ visual test, where channels satisfying $\Delta\mathrm{BT} > 3 \times$ NEDT indicate robust detectability.
These scenario-based results complement the controlled SO_2 sweep analysis in the following subsection. The scenario analysis demonstrates how realistic Hunga Tonga plume configurations alter the spectral SO_2 signal and its channel-wise SNR relative to IASI noise.

3.3 Controlled SO_2 detection limit comparison: Clean vs Scattering

Figure 3 represents the controlled SO_2 detection analysis using two systematically varied run sets. The clean reference signal is defined according to Equation 2, while the scattering signal is defined by Equation 1. For each SO_2 amount (DU), the metric used is the peak absolute differential signal within the SO_2 absorption window (1000–1200 cm^{-1}). The channel-dependent IASI NEDT, interpolated onto the SRFM grid, is then used to calculate the corresponding peak SNR values, with detection assessed at 3σ threshold as previously discussed.
The left axis shows peak $|\Delta\mathrm{BT}|$ versus SO_2 amount for the clean and scattering cases (solid lines), while the right axis shows peak SNR for the same runs (dashed lines). Across sampled SO_2 values (10, 20, 25, 30, 50 DU), peak SNR increased in both clean and scattering cases but remained lower in runs where scattering was included.
Linear interpolation between sampled DU points gives an estimated 3σ crossing at 11.7 DU for the clean configuration, and 14.6 DU for the scattering configuration. This implies that scattering increases the effective SO_2 detection limit by approximately 2.9 DU under the tested conditions. The controlled sweep therefore demonstrates a clear, quantitative suppression of detectable SO_2 signal by scattering in the IASI infrared SO_2 window.

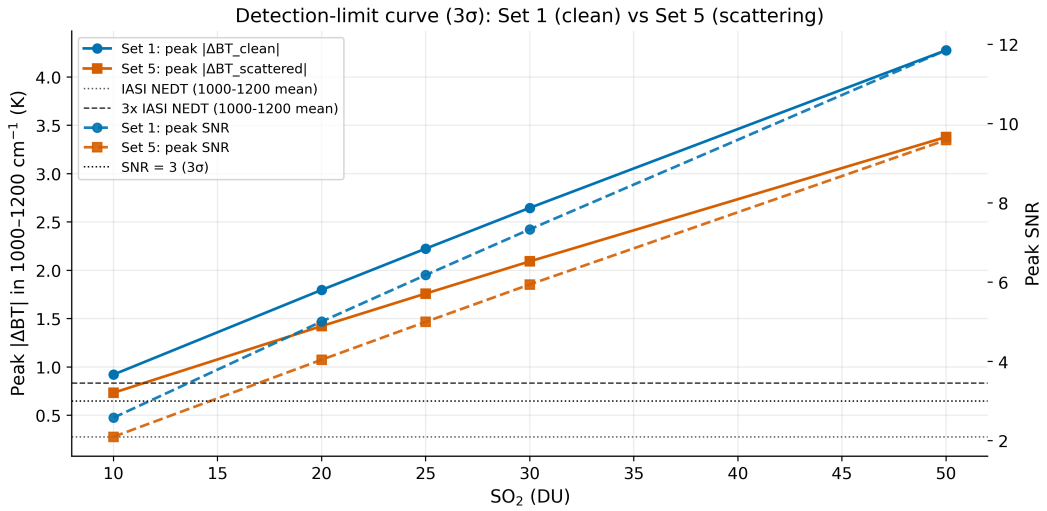

Figure 3: Detection limit curves for the clean (Set 1, B−D) and scattered (Set 5, A−C) SO_2 sweeps. Left axis: peak $|\Delta BT|$ in the 1000–1200 cm^{-1} window as a function of SO_2 column amount. Right axis: corresponding peak SNR. Horizontal lines mark the mean IASI NEDT and the 3σ detection threshold in the analysis window. The 3σ crossing points define the clean and scattered detection limits.

3.4 Hunga Tonga scenario detectability

To assess SO_2 detectability for Hunga Tonga, scenario-specific metrics were evaluated separately from the controlled SO_2 sweep. Figure 4 shows the peak window $|\Delta BT|$ and SNR for the four different Hunga Tonga cloud scenarios modelled.

The scenario comparison indicates that detectability depends on plume configuration as well as SO_2 concentration. The scenario results are:

1. Scenario 6.1 (30 DU): peak $|\Delta BT| = 2.21$ K, peak SNR = 6.30
2. Scenario 6.2 (30 DU): peak $|\Delta BT| = 2.08$ K, peak SNR = 5.91
3. Scenario 6.3 (10 DU): peak $|\Delta BT| = 0.78$ K, peak SNR = 2.23
4. Scenario 6.4 (30 DU): peak $|\Delta BT| = 2.20$ K, peak SNR = 6.26

Using the 3σ detection criterion, scenarios 6.1, 6.2 and 6.4 are detectable, while scenario 6.3, which models the plume edge, is below the threshold. This shows that the lower SO_2 case is noise-limited under the tested scattering conditions.

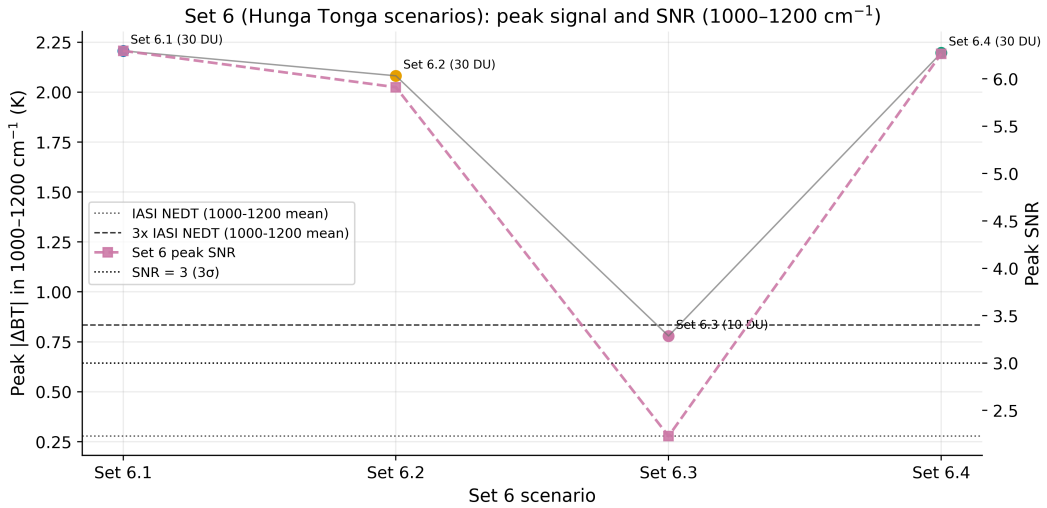

Figure 4: Peak $|\Delta BT|$ in the 1000–1200 cm^{-1} window for each Set 6 Hunga Tonga scenario. The dashed black line marks the 3σ detection threshold. Scenario 6.3 (10 DU) falls below the detection threshold; scenarios 6.1, 6.2 and 6.4 (30 DU) are detected comfortably.

3.5 Sensitivity to aerosol properties at fixed SO_2

Figure 5 shows the scattering loading sensitivity at fixed SO_2, using $|\Delta BT|$ signal. The plotted metric is the peak $|\Delta BT|$ in the SO_2 window.

In Figure 5, the sulphuric acid sweep (0.01–1.0 g m^{-2}) shows a clear reduction in signal strength, with peak $|\Delta BT|$ decreasing from 2.61 K to 2.12 K. The ash sweep has similar results, with the peak

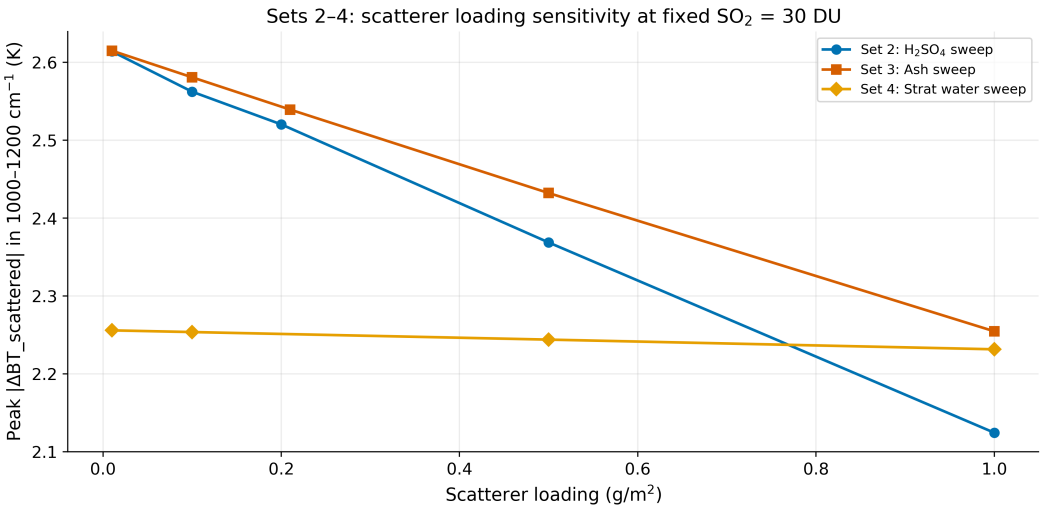

Figure 5: Peak $|\Delta BT|$ in the 1000–1200 cm^{-1} window as a function of scatterer mass loading at a fixed SO_2 column of 30 DU, for H_2SO_4, ash and stratospheric water ice.

also decreasing over the range, from 2.62 K to 2.23 K. By contrast, the mass loading sweep of the stratospheric water cloud shows a weak response over 0.01 to 1.0 g m^{-2}, with peak $|\Delta BT|$ changing by 0.024 K over the range.

This indicates that sulphuric acid loading produces the strongest suppression of SO_2 window signal within the tested range, with ash producing a moderate suppression, and the stratospheric water cloud having little effect.

4 Discussion

4.1 Clean Atmosphere Detection Limit

The controlled SO_2 sweep in the absence of scattering establishes a baseline detection limit of 11.7 DU at the 3σ threshold (Figure 3). Below this column amount, the SO_2 absorption feature in the 1000–1200 cm^{-1} window is indistinguishable from IASI noise, when injected between 23 and 25 km.

Across the full simulated range of 10–50 DU, the peak $|\Delta BT|$ scales almost proportionally with SO_2 column amount. The ratio of successive peak $|\Delta BT|$ values matches the corresponding SO_2 ratio to within 3% at every increment, indicating that the signal remains well within the optically thin regime. This linearity holds across the simulated range of 10–50 DU, but it would be expected to break down at higher SO_2 column amounts. As the absorption lines approach saturation, incremental increases in column amount produce diminishing returns in $|\Delta BT|$, and the signal growth transitions from linear to sub-linear. The simulated range is therefore safely within the regime where column amount and signal are directly proportional, simplifying interpretation of the detection threshold.

4.2 Impact of Scattering on the Detection Limit

Introducing a realistic volcanic scattering layer shifts the 3σ detection threshold from 11.7 DU to 14.6 DU, an increase of 2.9 DU (approximately 25%) (Figure 3). This is expected on physical grounds, as scattering redistributes photons out of the direct line of sight, effectively diluting the gas absorption signature and reducing the spectral contrast.

Despite the upward shift, the detection limit curve retains the same overall shape and near-linear growth rate at the modest SO_2 loadings modelled. This indicates that scattering attenuates the overall magnitude of the SO_2 signal without distorting its spectral shape. The consequence of this is that a retrieval algorithm tuned to a clean atmosphere would still recognise the spectral signature of SO_2 in the presence of volcanic aerosol, but would systematically underestimate the column amount, or fail to flag the marginal SO_2 concentration in the edges of the plume, near the detection threshold. A 25% elevation of the detection limit is modest in the context of large eruptions, where SO_2 columns of hundreds of DU are common, but it becomes significant for smaller eruptions, late-stage dispersed plumes and plume edges, where column amounts are near the detection boundary. In such cases, neglecting scattering could result in SO_2 signals being missed.

It should be noted that these detection limits are specific to the peak channel-wise $|\Delta BT|$ metric used throughout. The SO_2 absorption feature spans many channels, and as shown in Figure 6, the integrated SNR across the ν_1 window remains substantial even at column amounts where no individual channel exceeds the 3σ threshold. A detection criterion based on integrated SNR or on counting channels

exceeding 3σ would therefore yield a lower effective detection limit than the peak-channel values of 11.7 DU and 14.6 DU reported here. The relative 2.9 DU shift between the clean and scattered cases is robust across all three metrics, reinforcing the conclusion that scattering produces a consistent and quantifiable suppression of the detectable SO_2 signal, independent of the choice of detection criterion.

4.3 Spectral Character of the Scattering Perturbation

The paired difference spectra for the Hunga Tonga scenarios (Figure 1) illustrate how scattering modifies the observed $|\Delta BT|$ signal. Comparing $|\Delta BT_{scattered}|$ and $|\Delta BT_{clean}|$ for the central Hunga Tonga scenario shows that the SO_2 absorption trough between 1100 and 1170 cm^{-1} is attenuated by the scattering layer.

Outside the analysis window, the full spectrum view (Figure 2) reveals a second, considerably stronger absorption feature between approximately 1310 and 1395 cm^{-1}, peaking near 1360 cm^{-1}. This is the SO_2 ν_3 asymmetric stretching band, which at 30 DU produces a peak ΔBT of 11.3 K, approximately 4 times larger than the corresponding signal in the ν_1 region. Notably, the ν_3 feature is nearly identical in amplitude in both the scattered and clean difference spectra (11.3 K and 11.5 K, respectively). The analysis is focused on the ν_1 window, in part because the stronger ν_3 band overlaps significantly with water vapour absorption. In the case of Hunga Tonga, this overlap is problematic, due to the exceptional mass of water vapour injected into the stratosphere, producing anomalously strong water absorption that partially obscures the ν_3 SO_2 signal. Reliable use of the ν_3 band therefore requires prior characterisation of the water vapour content and its spectral absorption within the plume, providing an additional source of uncertainty not present in the ν_1 analysis.

Within the 1000–1200 cm^{-1} window (Figure 2), the $|\Delta BT|$ curves for the 30 DU scenarios (6.1, 6.2, 6.4) comfortably exceed the $3 \times$ NEDT envelope, confirming detection above the 3σ threshold. In contrast, the plume-edge scenario with a SO_2 column amount of 10 DU (6.3) barely reaches the $3 \times$ NEDT boundary; its peak SNR of 2.23 (Figure 4) falls below the detection criterion, demonstrating that a moderate plume or plume-edge scenario, in the presence of Hunga Tonga-like scattering, would not be detected by IASI.

4.4 Sensitivity to Individual Scatterers

Figure 5 isolates the effect of the mass loading of each scatterer type at a fixed SO_2 column of 30 DU, injected between 23 and 25 km. Of the three species tested, H_2SO_4 aerosol produces the largest suppression of the SO_2 signal, reducing the peak $|\Delta BT|$ from 2.61 K to 2.12 K (difference of 0.49 K) as the loading increases across the sweep range. Volcanic ash also has a moderate effect, with a reduction of 0.36 K across the sweep range. The stratospheric water modelled from 26–27 km has a negligible effect on the observed SO_2 signal, decreasing by 0.024 K.

The dominance of the H_2SO_4 aerosol is physically reasonable. Sulphuric acid aerosol forms rapidly in the stratosphere following SO_2 injection [2] and has strong, spectrally smooth extinction across the thermal infrared that directly competes with the gas-phase SO_2 absorption. Its refractive index in the thermal infrared gives rise to significant extinction, through both absorption and scattering, across the 830–1250 cm^{-1} window [17], directly suppressing the observed SO_2 signal. Ash, though more opaque, tends to sediment from the stratosphere on much shorter timescales [18], with only small particles remaining, and is therefore less persistent as an interference.

The low sensitivity to stratospheric water ice is consistent with the relatively small optical depths expected for ice at those wavenumbers, compared with sulphuric acid or ash particles.

4.5 Hunga Tonga Scenario Analysis

The four Set 6 scenarios represent plausible atmospheric states during the January 2022 Hunga Tonga eruption, each combining different scatterer compositions and concentrations of 30 DU or 10 DU of SO_2. Peak SNR values (Figure 4) are: 6.30 (Set 6.1), 5.91 (Set 6.2), 2.23 (Set 6.3) and 6.26 (Set 6.4). Three of the four scenarios comfortably exceed the 3σ threshold, indicating that IASI would reliably detect the 30 DU SO_2 plume even with the complex mixture of H_2SO_4, ash and water aerosol that characterised the Hunga Tonga plume. The plume-edge scenario, 6.3, however, with its reduced 10 DU column, falls below the detection limit (SNR = 2.23). This is consistent with the controlled sweep, which placed the scattering detection limit at 14.6 DU, well above 10 DU.

The comparison between the 30 DU scenarios reveals that the specific scatterer composition only produces modest variation in peak SNR (5.91–6.30). This suggests that once the SO_2 column is well above the detection threshold, the precise aerosol mixture matters less than the total scattering optical depth.

4.6 Limitations

There are a few limitations to the analysis that are due to the current modelling framework. One of these is the single-layer geometry of the SRFM, as it treats the scattering layers and gas absorption as single stratospheric slabs. In reality, vertical separation between the SO_2 plume and the aerosol layers would modulate the scattering interference, potentially increasing or decreasing the signal.
Another limitation is that all simulations assume nadir geometry. At higher viewing angles, the optical path through gas and aerosol layers increases, enhancing the SO_2 signature and scattering extinction. The net effect on detection limits could therefore be different when viewed at off-nadir angles.
Each simulation is run using a single daytime tropical atmosphere, taken from the MIPAS model atmosphere for January 2001. While the CO_2 amounts have been adjusted to 2022 levels as discussed, this scenario is still not representative of the exact atmospheric conditions near Hunga Tonga in 2022, decreasing the accuracy of the volcanic scenario simulations. Additionally, there would be variations in surface temperature and humidity, which would contribute additional noise to satellite retrievals.
Despite these simplifications, the forward model approach captures the essential physics of the scenarios and allows individual sensitivities to be isolated cleanly.
Several simulation scenarios were not fully explored within the scope of this project. The relative vertical ordering of the SO_2 and scattering layers was partially investigated, and preliminary results suggested that the ordering of the scattering layers has little effect on the retrieved $|\Delta BT|$ signal; however, this was not explored systematically across all parameters. More significantly, the sensitivity of the detection limit to the absolute altitude of the SO_2 layer was not investigated: placing the SO_2 column below, within, or above the scattering layer would alter the effective optical path through both media and could plausibly change the magnitude of the scattering suppression. Extension to the UV regime, to compare SO_2 detection sensitivity between UV and infrared channels under optically thick scattering conditions, has also not been explored. This would allow for direct comparison of how the two regimes are affected by volcanic aerosol and would assess how detection sensitivity in the UV compares to the infrared under heavy scattering conditions. This and the vertical structure questions represent the most important direction of future work.

4.7 Implications for operational SO_2 modelling

The results have several direct implications for satellite-based SO_2 monitoring of volcanic eruptions. Most immediately, satellite retrievals that assume a scattering-free atmosphere will underestimate the minimum detectable SO_2 column by approximately 25% in the presence of volcanic scatterers. Applying a correction for this would improve detection reliability for marginal plumes, where the distinction between detected and undetected signals depends on how accurately the background scattering state is characterised.
The sensitivity analysis demonstrates that this correction is not equally important for all scatterer types. H_2SO_4 aerosol is by far the dominant source of signal suppression of those modelled, outweighing ash and stratospheric water ice across the loadings tested (Figure 5). This implies that accurate characterisation of sulphuric acid aerosol optical depth is more important than ash or ice for SO_2 retrieval purposes, and that retrieval methods should prioritise sulphuric acid aerosol constraints when processing data from sulphur-rich eruptions.
The consequence is particularly significant for threshold plumes where SO_2 columns hover near the detection boundary, such as small eruptions, plume edges or late-stage dispersed plumes. The approximate 3 DU shift may be modest in absolute terms, but it corresponds to a substantial fraction of the total detectable range at low concentrations.
In the specific context of Hunga Tonga, the dominance of H_2SO_4 suppression points to an important observational correction. The eruption injected large amounts of water vapour into the stratosphere [2], which rapidly accelerated the conversion of SO_2 to sulphuric acid aerosol. As such, scattering-induced suppression of the SO_2 signal would grow in the days following the eruption. Notably, the simulations show that stratospheric water ice itself has a negligible direct effect on SO_2 detectability, so the primary radiative interference from the water injection is indirect, instead acting through the sulphuric acid aerosol it helps produce. Beyond this indirect effect, stratospheric water vapour has strong absorption features of its own throughout the thermal infrared, including within the SO_2 ν_1 window, adding a further layer of spectral complexity to SO_2 retrievals from this eruption.

5 Conclusion

This project has quantified the effect of volcanic aerosol scattering on the detection limit of SO_2 in the infrared, using the SRFM to simulate IASI brightness temperature spectra across a controlled range of SO_2 column amounts and scattering configurations motivated by the January 2022 Hunga Tonga

eruption.
In a clean atmosphere, the IASI ν_1 window (1000–1200 cm^{-1}) yields a 3σ detection limit of 11.7 DU for a stratospheric SO_2 layer injected between 23 and 25 km. The signal scales linearly with column amount to within 3% across the full simulated range of 10–50 DU, confirming operation in the optically thin regime. Introducing a volcanic scattering layer based on Raikoke aerosol observations raises this threshold to 14.6 DU, an increase of 2.9 DU, or approximately 25%. Scattering attenuates the signal amplitude without shifting the spectral features, meaning the SO_2 signature remains identifiable, but columns near the detection limit risk being missed entirely due to instrument noise.
Of the three scatterer species examined, H_2SO_4 aerosol dominates the signal suppression, reducing peak $|\Delta BT|$ by 0.49 K across the mass loading range tested. Volcanic ash has a moderate effect (0.36 K), and stratospheric water ice's effect on the spectrum is negligible. This directly informs retrieval strategy, showing that accurate characterisation of sulphuric acid aerosol loading is the most critical scattering correction for SO_2 retrievals from sulphur-rich eruptions.
Applied to the Hunga Tonga eruption, all three 30 DU plume scenarios comfortably exceed the 3σ threshold (SNRs of 6.30, 5.91, and 6.26), demonstrating that IASI should reliably detect the core plume even under the complex mixed scattering environment of the eruption, at the loadings used. The plume-edge scenario with 10 DU falls below the detection threshold (SNR = 2.23), consistent with the controlled detection limit of 14.6 DU, and illustrating that dispersed or marginal plumes remain noise-limited under heavy scattering. The near-identical SNRs of the three 30 DU scenarios, despite varying aerosol compositions, indicate that well above the detection threshold the total scatterer loadings matter more than the precise mixture of scatterers.
The analysis is subject to the limitations of single-layer plane-parallel geometry, nadir-only viewing, and a single tropical background atmosphere. The most important directions for future work are a systematic investigation of SO_2 layer altitude relative to the scattering layers, extension to the stronger SO_2 ν_3 band (1310–1395 cm^{-1}) and expansion to the UV regime to enable direct comparison with TROPOMI observations.

References

[1] Alan Robock. "Volcanic Eruptions and Climate". In: *Reviews of Geophysics* 38.2 (2000), pp. 191–219. DOI: 10.1029/1998RG000054.

[2] P. Sellitto et al. "Unexpectedly large stratospheric aerosol mass from Hunga Tonga-Hunga Ha'apai eruption". In: *Geophysical Research Letters* (2023). DOI: 10.1029/2023GL105565.

[3] Roy Grainger and Antonin Knizek. *SRFM*. n.d. URL: https://github.com/eodg-code/srfm.

[4] Cathy Clerbaux et al. "Monitoring of atmospheric composition using the thermal infrared IASI/MetOp sounder". In: *Atmospheric Chemistry and Physics* 9 (2009), pp. 6041–6054. DOI: 10.5194/acp-9-6041-2009.

[5] A. Dudhia. "The Reference Forward Model (RFM)". In: *Journal of Quantitative Spectroscopy and Radiative Transfer* (2017).

[6] K. Stamnes et al. "Numerically stable algorithm for discrete-ordinate-method radiative transfer in multiple scattering and emitting layered media". In: *Applied Optics* 27.12 (1988), pp. 2502–2509. DOI: 10.1364/AO.27.002502.

[7] I. E. Gordon et al. "The HITRAN2020 molecular spectroscopic database". In: *Journal of Quantitative Spectroscopy and Radiative Transfer* 277 (2022), p. 107949. DOI: 10.1016/j.jqsrt.2021.107949.

[8] *ARIA Aerosol Refractive Index Archive*. n.d. URL: https://eodg.atm.ox.ac.uk/ARIA/.

[9] Bernard Legras et al. "The Hunga Tonga-Hunga Ha'apai eruption: transport and fate of the plume". In: *Atmospheric Chemistry and Physics* 22 (2022), pp. 14957–14974. DOI: 10.5194/acp-22-14957-2022.

[10] J. J. Remedios et al. "MIPAS reference atmospheres and comparisons with MIPAS level 2 data". In: *Atmospheric Chemistry and Physics* 7 (2007), pp. 1209–1220. DOI: 10.5194/acp-7-1209-2007.

[11] L. Millán et al. "Water vapor injection into the stratosphere by Hunga Tonga-Hunga Ha'apai". In: *Science* 377 (2022). DOI: 10.1126/science.abq2299.

[12] *NOAA Global Monitoring Laboratory CO2 Trends*. 2023. URL: https://gml.noaa.gov/ccgg/trends/.

[13] C. Raymond et al. "Atmospheric effects of the Tonga volcanic sulfate aerosols". In: *Journal of Volcanology and Geothermal Research* (2024).

[14] L. Muser et al. "Particle aging and aerosol–radiation interaction affect volcanic plume dispersion: Evidence from Raikoke eruption 2019". In: *Atmospheric Chemistry and Physics* 20 (2020), pp. 15015–15036. DOI: 10.5194/acp-20-15015-2020.

[15] S. Bekki. "Oxidation of volcanic SO2: A sink for stratospheric OH and H2O". In: *Geophysical Research Letters* 22 (1995), pp. 913–916. DOI: 10.1029/95GL00534.

[16] L. Clarisse et al. "Retrieval of sulphur dioxide from the infrared atmospheric sounding interferometer (IASI)". In: *Atmospheric Chemistry and Physics* 12 (2012), pp. 11417–11434. DOI: 10.5194/acp-12-11417-2012.

[17] A. Eldering et al. "Vertical profiles of aerosol extinction from infrared measurements". In: *Applied Optics* (1994).

[18] W. I. Rose and A. J. Durant. "Fate of volcanic ash: Aggregation and fallout". In: *Geological Society of America Special Papers* (2011).

A Alternative Detection Metrics

Figure 6 shows two alternative detection metrics computed across the SO_2 ν_1 window (1000–1200 cm^{-1}) for the clean (Set 1, B-D) and scattered (Set 5, A-C) column sweeps: the number of channels independently exceeding the 3σ threshold (left), and the integrated SNR ($\sqrt{\sum_i (\Delta BT_i/\sigma_i)^2}$, right). Both metrics preserve the clean/scattered ordering at all tested column amounts, confirming that the 2.9 DU shift reported in Section 3.3 is robust to the choice of detection criterion.

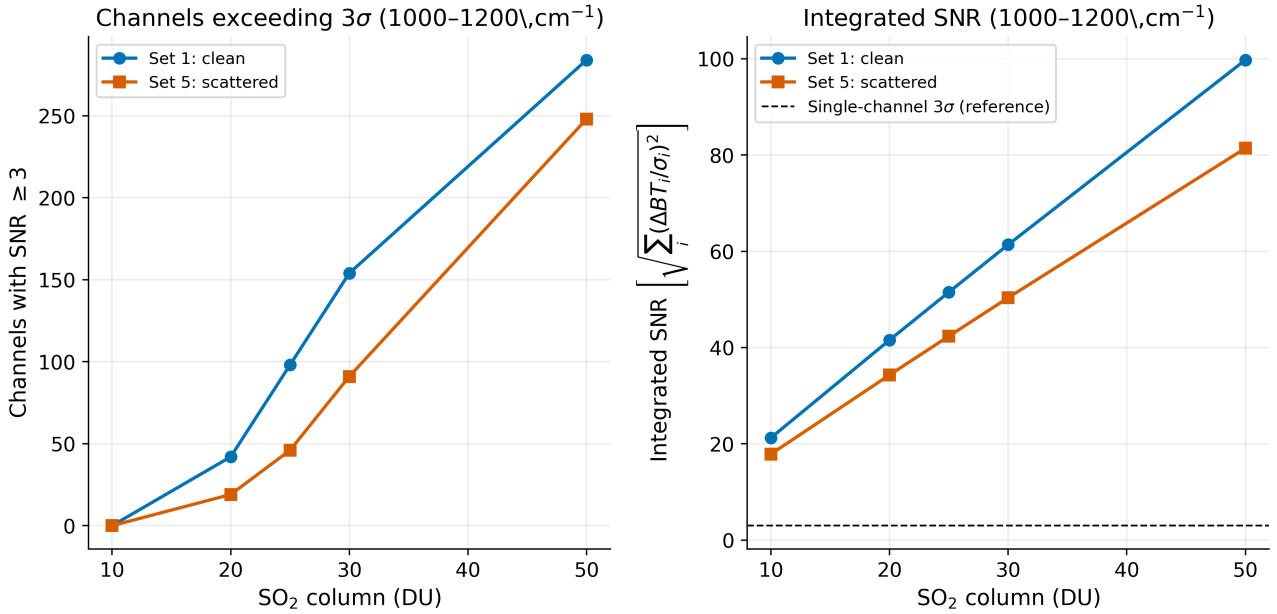

Figure 6: Alternative detection metrics for the clean (Set 1, B-D) and scattered (Set 5, A-C) SO_2 column sweeps. *Left:* number of channels independently exceeding the 3σ detection threshold in the 1000–1200 cm^{-1} window. *Right:* integrated SNR ($\sqrt{\sum_i (\Delta BT_i/\sigma_i)^2}$) across the same window; the dashed line marks the single-channel 3σ level for reference only—the true detection threshold for the integrated metric is higher and depends on the number of channels. Both metrics confirm that scattering consistently suppresses the detectable SO_2 signal, and that a multi-channel criterion would yield a lower effective detection limit than the peak-SNR values quoted in the main text.